Journal of Materials Chemistry A

ROYAL SOCIETY OF CHEMISTRY

PAPER

View Article Online
View Journal | View Issue

Check for updates

Cite this: J. Mater. Chem. A, 2025, 13, 7476

Dual protective layer on lithium metal anodes for improved electrochemical performance – in-depth morphological characterization†

Marlena M. Bela,[a] Maximilian Mense,[a] Sebastian Greiwe,[a] Marian C. Stan,[b] Simon Wiemers-Meyer,[a] Martin Winter[ab] and Markus Börner *[a]

Lithium metal is a promising electrode material to increase the specific energy and energy density of rechargeable batteries. The high reactivity of lithium in contact with the electrolyte leads to the formation of a solid electrolyte interphase (SEI) that is inhomogeneous in composition and morphology. The SEI is prone to cracking due to volume changes and favors high surface area lithium growth, pit formation and an accelerated Li bulk consumption during electrodeposition/-dissolution due to continuous SEI regeneration. These drawbacks result in low coulombic efficiency and cycle life, and pose a safety risk to rechargeable lithium metal batteries with liquid electrolytes that must be addressed before commercialization. Protective layers by *ex situ* surface modifications are an attractive strategy to improve the cycle life and performance of lithium metal batteries as they mitigate Li metal degradation reaction and homogenize the Li ion transport from/into electrolyte. Herein, a dual protective layer consisting of an intermetallic LiZn and inorganic Li_3N layer deposited by thermal evaporation was investigated. A deeper insight into the durability of the dual protective layer was gained by cross-sections under cryogenic conditions before and after electrodeposition/-dissolution. Galvanostatic cycling experiments in symmetric Li||Li cells revealed an increase in cycle life of 80% and the state of health from $LiNi_{0.6}Mn_{0.2}Co_{0.2}O_2$||Li cells was improved by 50% (SOH 80) for Li electrodes with a dual protective layer compared to pristine Li metal.

Received 6th September 2024
Accepted 10th January 2025

DOI: 10.1039/d4ta06366j

rsc.li/materials-a

Open Access Article. Published on 14 januar 2025. Downloaded on 28.8.2025 23:04:52.
This article is licensed under a Creative Commons Attribution 3.0 Unported Licence.

Introduction

Li ion batteries (LIBs) are approaching their theoretical and practical limit in specific energy and there are rising concerns that they will meet the increasing demand for various mobile and stationary applications.[1–3] Li metal as active material for the negative electrode is a promising candidate for rechargeable next generation battery systems to meet these demands, since Li has the highest capacity (3860 mA h g^{-1}) and lowest electrode potential (−3.04 V *vs.* standard hydrogen electrode).[4,5] The high reactivity of Li metal towards liquid organic electrolytes leads to electrolyte decomposition products that form a solid electrolyte interphase (SEI) on the Li metal surface, which is inhomogeneous in composition and morphology.[6,7] The heterogeneous interphase consists of different domains of decomposition products which were firstly described by E. Peled with a mosaic model.[8] Between the domains are grain boundaries, which allow faster Li ion diffusion, predisposing to pit formation and various morphologies of high surface area lithium (HSAL, with dendritic Li being the most prominent morphology) growth during electrodeposition/-dissolution.[7,9,10] During continuous electrodeposition/-dissolution, the thickness of the HSAL layer increases and inactive "dead" Li is formed, causing low coulombic efficiency, rapid capacity decay and serious safety issues.[11,12] In response to these challenges, various strategies were developed to reduce HSAL growth, including the addition of additives to electrolytes,[13,14] the creation of artificial 3D structures,[15,16] and the application of protective surface layers through *in* and *ex situ* surface modifications. These approaches aim to design an artificial protective layer that homogenizes and facilitates Li ion diffusion, prevents further reactions between the Li surface and the electrolyte, and remains stable and effective during electrodeposition/-dissolution.[17,18] *Ex situ* coatings have the advantage that their layer thickness and composition are easier to control. As a result, extensive studies have been conducted on organic, inorganic and intermetallic layers on Li metal to evaluate their protection properties.[19,20] Organic layers benefit from their mechanical flexibility and possibility to withstand volume changes of the electrode during charge/discharge, but lack in acceptable Li ion conductivity compared to inorganic and intermetallic layers.[21] Inorganic

[a]MEET Battery Research Center, University of Münster, Corrensstraße 46, 48149 Münster, Germany. E-mail: markus.boerner@uni-muenster.de
[b]Helmholtz-Institute Münster, IMD-4, Forschungszentrum Jülich GmbH, Corrensstraße 46, 48149 Münster, Germany

† Electronic supplementary information (ESI) available. See DOI: https://doi.org/10.1039/d4ta06366j

This journal is © The Royal Society of Chemistry 2025

Open Access Article. Published on 14 januar 2025. Downloaded on 28.8.2025 23:04:52.
This article is licensed under a Creative Commons Attribution 3.0 Unported Licence.

layers, such as Li_3N, provide a high Li ion conductivity (10^{-3} S cm^{-1}), low electronic conductivity (>10^{-12} S cm^{-1}) and (electro-)chemical stability against Li, resulting in an attractive coating material for Li metal batteries (LMBs).[22–25] However, nanoscale Li_3N layers suffer from poorly interconnected Li_3N grains, that lead to coating cracks at grain boundaries during cycling and subsequently facilitated HSAL growth. A pinhole-free Li_3N layer was proposed that improved the electrodeposition/-dissolution behavior, but the observed performance improvement was presumably due to a several microns thick Li_3N layer.[26]

Intermetallic layers show a noteworthy reduction in overvoltage and in Li metal reactivity towards the electrolyte, and as a result a homogeneously distributed electrodeposition behavior of Li ions.[27–29] Nevertheless, HSAL deposition on the surface, attributed to the electronic conductivity of the intermetallic layer was observed, along with coating cracks and accelerated HSAL growth in these regions during cycling. Additionally, the dissolution of the intermetallic layer into HSAL and Li bulk was occurring.[29,30]

While single protective layers are a viable strategy to overcome specific challenges, they do not offer a comprehensive solution for simultaneously enhancing energy and power performance, cycle life, and safety – key factors needed for the successful application of rechargeable LMBs. Consequently, a combination of artificial layers that meet several requirements for an optimal protective layer was investigated. A combination of an intermetallic layer to provide uniformly distributed nucleation sites for Li ions and an inorganic layer to block the electron transport and ensure the Li ion deposition underneath the protective layer was recently investigated.[31–34] Here, liquid-phase reactions were used for surface modification, although the layer thickness is difficult to control.[32,33] A dual protective layer based on thermal evaporation was investigated for solid-state batteries with a LiF/LiAg coating showing a considerable enhancement in cycling performance and stability.[31] The effective combination of an intermetallic and inorganic layer led to the encouragement of engineering a dual protective layer by thermal evaporation. Hence, a dual protective layer composed of an intermetallic LiZn and an inorganic Li_3N layer deposited by thermal evaporation and subsequent gas reaction in the chamber is presented. Thermal evaporation is a physical vapor deposition (PVD) technique that produces high purity coatings, due to solvent- and organic free fabrication of thin films under high vacuum, and is more cost- and energy efficient compared to other PVD techniques.[35–37] The thickness control during the coating process is adjustable, as recently demonstrated for an intermetallic LiZn layer.[29] Zinc deposition was chosen to create an intermetallic LiZn layer due to its high Li ion diffusion coefficient, homogeneous distributed Li ion nucleation sites, low cost and toxicity.[38–40] Li_3N has a high Li ion and low electron conductivity, and is therefore a suitable protective layer on top of the intermetallic layer to reduce electronic leakage. Integrating a dual protective layer on Li electrodes is expected to effectively improve the cycle life and performance in Li||Li and NMC622||Li cells compared to single coated or uncoated Li electrodes. To gain a comprehensive insight into the beneficial behavior of the protective layer during cycling, *post mortem* analysis of cycled electrodes was conducted with a morphology preserving technique.

Experimental

Materials

Battery grade Li metal was purchased from Honjo Lithium in a thickness of 500 μm and was roll-pressed to a final thickness of 130 μm (Li_{rp}) between two siliconized polyester foils (50 μm, PPI Adhesive Products GmbH) using a roll-press calendar (GK300L, Saueressig) in a dry room (dew point <−60 °C). The roll-pressing method was employed to reduce the surface roughness and dilute the native layer, consisting of Li_2CO_3, LiOH and Li_2O.[41–43] Li_{rp} were then transferred to an Ar-filled glovebox (H_2O and O_2 values <0.1 ppm) for coating or electrode preparation under inert atmosphere. Zinc (Zn) pellets (Sigma Aldrich) with a purity of 99.99% were purchased to form the LiZn-intermetallic layer, and nitrogen gas (N_2, Westfalen AG) with a purity of 99.999% was purchased to produce the Li_3N layer.

Physical vapor deposition by thermal evaporation

The coating process was performed in a ProVap PVD System (MBraun) chamber placed in an Ar-filled glovebox (H_2O and O_2 values <0.1 ppm). This system is based on a resistive heating approach, where a high electric current and low voltage is applied to melt and vaporize the source material. An SQC-310 thin film deposition controller (Inficon) operating at 6 MHz was used to control the deposition rate during the evaporation process. The substrate was protected by a shutter until the desired deposition rate was reached and a shutter above the deposition material protects the substrate against out-gassing. Li_{rp} metal foil (130 μm) was placed on the substrate holder inside the PVD chamber facing downwards to the evaporation source to deposit different thicknesses at a rate of 0.5 nm s^{-1}. For the deposition process, Zn pellets were placed in a tungsten evaporation boat and Li in a tantalum evaporation boat, both connected to a power supply. To obtain a Li_3N layer, 100 nm Li was deposited on the Li_{rp} metal foil, and subsequently the PVD chamber was flooded with N_2 gas up to 500 mbar to allow the gas reaction between Li and N_2 to form Li_3N. The reaction was stopped after three min by evacuating the chamber. For the dual layer, 300 nm of Zn were deposited on the Li_{rp} metal foil to generate a LiZn-intermetallic layer followed by the Li_3N-layer fabrication process.

Electrochemical investigations

Li_{rp}, the single and dual layer protected electrodes were characterized in a CR2032-type two-electrode coin cell[44] for symmetric (Li||Li or LiZn||LiZn) and $LiNi_{0.6}Mn_{0.2}Co_{0.2}O_2$||Li (NMC622||Li, NMC622||LiZn) based cells and cycled at 20 °C using a MACCOR battery cycler (MACCOR series 4000). Symmetric coin cells were assembled in an Ar-filled glovebox (H_2O and O_2 values <0.1 ppm) using ∅ 12 mm Li electrodes and a ∅13 mm separator (2× Freudenberg (FS2190), 2× Celgard

Open Access Article. Published on 14 januar 2025. Downloaded on 28.8.2025 23:04:52.
This article is licensed under a Creative Commons Attribution 3.0 Unported Licence.

2500) soaked with 60 μL electrolyte containing 1 M $LiPF_6$ in EC/EMC (3 : 7 by weight, EC: ethylene carbonate, EMC: ethyl methyl carbonate). NMC622||Li cells were assembled under equivalent conditions, but a different cell setup was used including a ∅13 mm Li as negative electrode, ∅12 mm NMC622-based positive electrode and ∅14 mm separator soaked with 80 μL electrolyte. For symmetric cells the current density was varied from 0.5 mA cm^{-2} to 2 mA cm^{-2} with a constant capacity of 0.5 mA h cm^{-2} for long-term cycling experiments and cut-off criteria of −1.5 V to +1.5 V. The NMC622||Li cells were cycled after a rest period of 5 h in a voltage range of 3.0 V to 4.3 V at a charge/discharge rate of 0.2C (0.2 mA cm^{-2}, 1C corresponds to 180 mA g^{-1}). As positive electrode 95% NMC622 (BASF) as active material, 2% conductive additive (Super C65, IMERYS) and 3% polyvinylidene difluoride (PVDF) binder (Solef 5130, Solvay) was used to obtain positive electrodes with an areal capacity of 2.3 mA h cm^{-2} produced in an in-house battery line. The electrode sheets were pre-dried under vacuum (3×10^{-3} mbar) at 100 °C for 12 h and then punched into ∅12 mm electrodes.

Electrochemical impedance spectroscopy (EIS) was conducted using a VMP3 potentiostat (Bio-Logic) in a frequency range between 0.1 MHz and 0.1 Hz with an amplitude of 10 mV. For the EIS analysis combined with galvanostatic cycling symmetric Li||Li coin cells were used. Initially, EIS was measured three times under open circuit conditions (OCP) at 0 V. Thereafter, Li||Li cells were cycled at 0.5 mA cm^{-2} and 0.5 mA h cm^{-2} and EIS was conducted after each cycle for the first ten cycles and then after every fifth cycle up to 50 cycles.

Morphological investigation

The surface morphology of Li_{rp} and coated Li_{rp} before and after charge/discharge cycling was analyzed by scanning electron microscopy (SEM) using a Carl-Zeiss CrossBeam 550 working station with a field emission gun at an acceleration voltage of 3 kV. For SEM characterization, symmetric cells were disassembled after 20 and 50 cycles at 0.5 mA cm^{-2} to 0.5 mA h cm^{-2}. The samples were integrated inside an Ar-filled glovebox in a custom-built cryo-transfer module (Kammrath&Weiss), which was installed inside the SEM chamber and connected to liquid nitrogen and a temperature control element. The temperature was set at −160 °C and maintained for 10 min before the cross-section was started by focused ion bombardment (FIB). The cryo-conditions resulted in a morphological preservation of the Li metal and Li metal-containing structures, and the acceleration voltage of the FIB was 30 kV with a current ranging from 7 nA to 30 nA.

The elemental composition of the electrode surface and cross-section was investigated by energy-dispersive X-ray spectroscopy (EDX) using an Ultim Extreme detector from Oxford Instruments. The spectra were analyzed with the integrated AZtech software (Oxford Instruments) and recorded with an acceleration voltage of 5 kV and a current of 1 nA.

Time-of-flight secondary ion mass spectrometry (TOF-SIMS)

ToF-SIMS measurements were performed on a TOF.SIMS 5 instrument (Iontof GmbH) equipped with a 30 keV Bi primary ion source and a 2 keV Ar sputter ion source. For the analysis the primary ion source was tuned in the spectrometry mode (bunched mode) for high mass resolution. The analysis was performed in a 100 × 100 μm^2 field of view, scanned in random mode with 128 × 128 pixels and a cycle time of 60 μs. Bi_3^+ ions were used as primary ions with an ion current of 2.3 pA. During the measurement, the surface was sputtered with Ar^+ sputter ions at an ion current of 600 nA. Measurements were taken at different but comparable sample positions in both secondary ion polarities. For each sample a set of a minimum of three measurements at different positions was performed. Data evaluation was performed with SurfaceLab7.2 software (Iontof GmbH).[45]

Results and discussion

The fabrication of the single and dual protective layer with a deposited intermetallic LiZn and/or inorganic Li_3N layer is schematically illustrated in Fig. 1 and was conducted in a PVD chamber as depicted in Fig. S1.† First, Li metal foil was roll-pressed (Li_{rp}) to dilute the native layer, consisting predominantly of Li_2CO_3, LiOH and Li_2O components, and to decrease the surface roughness, as previously reported by Becking *et al.*[41,43,46] In a second step, an intermetallic LiZn or inorganic Li_3N layer was deposited on Li_{rp} by thermal evaporation. For the Li_3N layer fabrication, 100 nm Li were deposited on Li_{rp} under vacuum, followed by N_2 gas exposure. The freshly deposited, reactive Li quickly formed a Li_3N layer in N_2 gas atmosphere. After withdrawing the samples from the chamber, a red-brown color was observed on the Li metal surface indicating a successful coating procedure to fabricate a Li_3N layer (Fig. S2b;† $Li_{rp}|Li_3N$ layer further referred as LN and coated on a Li_{rp} electrode as Li_{LN}).[47–49] Intermetallic LiZn layers were thoroughly investigated in a previous report regarding the optimal thickness of the intermetallic layer and the effect of roll-pressing pristine Li foil before coating.[29] Especially the preceding roll-pressing showed a beneficial influence regarding the homogeneity of the coating

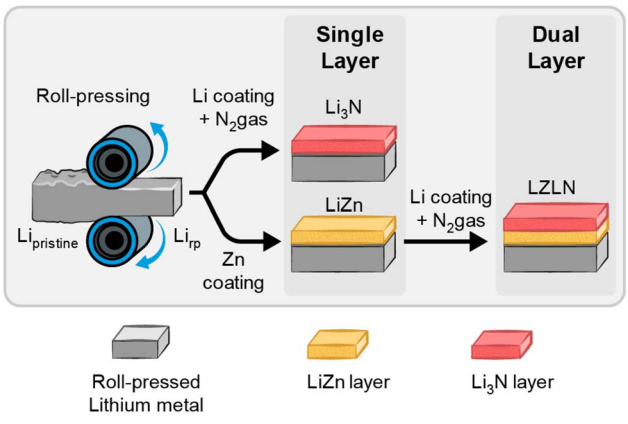

Fig. 1 *Ex situ* fabrication process for the dual protective layer starts with roll-pressing of Li metal foil to obtain Li_{rp} followed by PVD coating with either Zn or Li with subsequent N_2 exposure to obtain a single protective layer. An additional Li_3N layer is deposited on top of the LiZn-intermetallic layer to form the dual protective layer.

 This journal is © The Royal Society of Chemistry 2025

Open Access Article. Published on 14 januar 2025. Downloaded on 28.8.2025 23:04:52.
This article is licensed under a Creative Commons Attribution 3.0 Unported Licence.

morphology and an enhanced cycling performance by combining these methods. Based on these results, 300 nm Zn were deposited on Li_{rp} and considered as appropriate layer thickness to study the combination of an intermetallic LiZn and inorganic Li_3N layer and its behavior during electrodeposition/-dissolution. Fig. S2a† shows the intermetallic LiZn layer on Li_{rp} with a distinctive golden color, indicating the formation of an intermetallic phase.[27,28,30]

The dual protective layer on Li_{rp} electrodes (Li_{rp}|LiZn|Li_3N layer sequence further referred to as LZLN and coated on a Li_{rp} electrode as Li_{LZLN}) was fabricated by applying the two coating methods in sequence by depositing 300 nm Zn on Li_{rp} and subsequently 100 nm Li followed by exposure and reaction with N_2 gas. Therein, the deposition of 100 nm Li (prior to N_2 exposure) was determined as optimum in preliminary studies including Li thicknesses of up to 400 nm. The optical image of the LZLN layer Li_{rp} foil (Fig. S2c†) shows a homogeneous coating with a mixed golden and red-brown color. The advantage of this method is that the coatings are deposited under ultra-high vacuum, which prevents detrimental side reactions. In addition, thermal evaporation creates homogeneous coatings with a tunable layer thickness that can be adapted to the requirements of the cell chemistry. The Li_3N layer was chosen as top layer above the LiZn layer, due to its and electronic insulating properties, which promotes the deposition of Li ions under the protective layer.

The morphology, composition and thickness of the LN and LZLN layer were analyzed by SEM and EDX top-view and cross-section images and compared to the Li_{rp} reference surface (Fig. 2, corresponding EDX images: Fig. S3†). Cross-sections were performed under cryogenic conditions at −160 °C in order to preserve the morphology of the Li containing layers and the Li bulk by avoiding Li melting effects. SEM top-view images of Li_{rp} show linear grooved patterns from the roll-press method (Fig. 2a and b), but the overall surface roughness was reduced and the native layer was diluted compared to the pristine Li metal foil.[29,43] The corresponding cross-section image of Li_{rp} (Fig. 2c) presents a flat surface, which is essential for the subsequent coating process, as the surface roughness is forwarded to the applied coating. Fig. 2d–f displays the top-view and cross-section images of Li_{LN} and Fig. S3b and d† the corresponding EDX images. The top-view images show finely dispersed, well-connected particles of the LN layer on the Li_{rp} surface, and the corresponding EDX images reveal a homogeneous distribution of nitrogen. The thickness of the LN layer was determined from cross-section images to be 110 nm (Fig. 2f). Thus, the freshly deposited, highly reactive Li formed primarily with the induced N_2 gas and the subjacent Li_{rp} was not involved. The top-view and cross-section images of the Li_{LZLN} are demonstrated in Fig. 2g–i and the corresponding EDX images in Fig. S3f, g, i and j.† The top-view image in Fig. 2g shows a LZLN surface with a homogeneous coating and the formation of protrusions, that were caused by volume expansion during formation of the LiZn-intermetallic phase. After Zn deposition on Li foil (Zn: hcp structure; Li: bcc structure), Li atoms migrate into the Zn layer and form an intermetallic phase

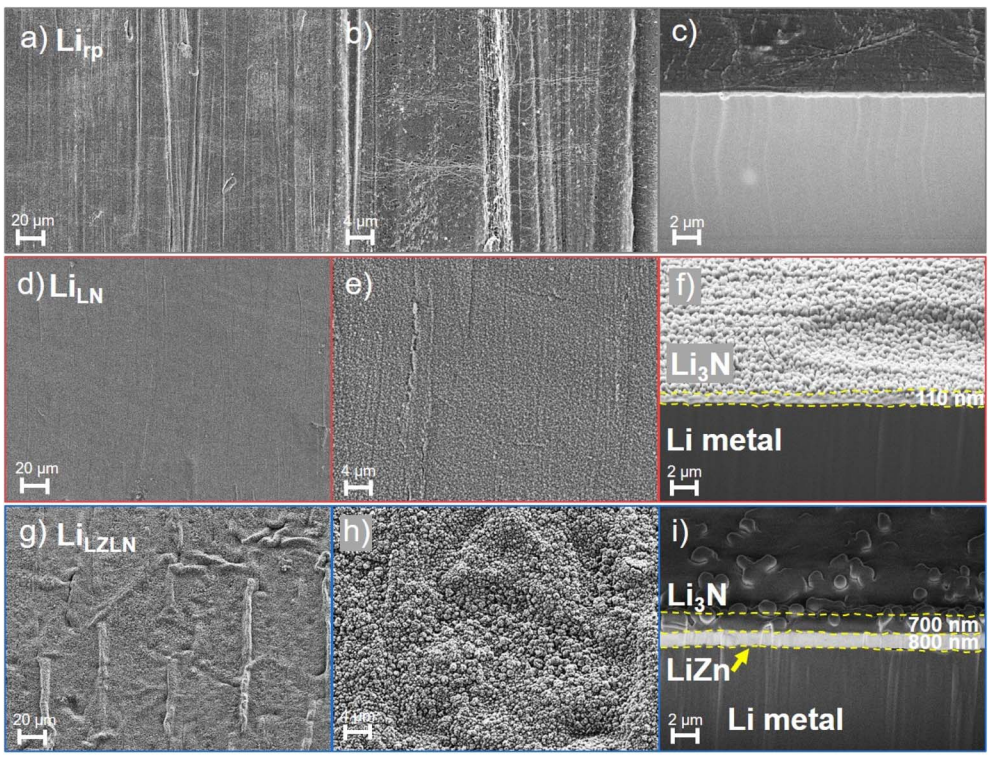

Fig. 2 Top view SEM images before cycling of (a) and (b) Li_{rp}, (d) and (e) Li_{LN} and (g) and (h) Li_{LZLN} electrodes. Cross-section images under cryogenic conditions of (c) Li_{rp}, (f) Li_{LN} at Li_{rp} and (i) Li_{LZLN}.

Open Access Article. Published on 14 januar 2025. Downloaded on 28.8.2025 23:04:52.
This article is licensed under a Creative Commons Attribution 3.0 Unported Licence.

(NaTl-type structure) resulting in volume expansion and curvature of the layer.[50] The cross-section image (Fig. 2i) confirms the volume expansion, indicating a layer thickness increase to 800 nm of the intermetallic LiZn layer with 300 nm of deposited Zn. Additionally, a distinct and homogeneous Zn signal was detected in the EDX cross-section image (Fig. S3j†). Moreover, it should be noted that beyond the flat Li_{rp} surface the deposition morphology of the LN layer is determined by the lattice structure and chemical properties of the corresponding substrate leading to different appearance in Fig. 2f (Li_{rp} substrate) and Fig. 2i (LiZn substrate) despite having the same chemical composition.

At higher magnifications, the LZLN layer shows connected grains over the entire surface. The corresponding EDX images confirmed the presence of Li_3N as top layer with detection of the nitrogen signal (Fig. 2h with corresponding EDX image in Fig. S3e and f†). However, areas with protrusions exhibited a reduction in the nitrogen signal and an increase in the zinc signal (Fig. S3f and g†). In flat regions, the LN layer is assumed to act as a shield, masking the zinc signal from the LiZn layer. In areas with protrusions, a higher signal intensity of zinc was detected by the EDX detector. The excitation bulb in areas with protrusions likely contains a higher quantity of zinc in the vicinity, which exceeds the detection limit for the nitrogen signal.

Consequently, the contrast between the nitrogen and the zinc signal in the respective regions was leading to the observation of an absence of the nitrogen signal. This is confirmed by the consistent structure of the LZLN layer in the top view images, which demonstrated a homogeneous distribution and well connected Li_3N grains (Fig. 2g and h). The cross-section image of the Li_{LZLN} (Fig. 2i) shows a consistent layer thickness of the LN layer with a thickness of 700 nm on top of the LiZn layer compared to 110 nm LN layer on the Li_{rp} surface. The thickness determination was conducted in an additional cross-section with a platinum layer on top of the LZLN layer to exclude the potential co-measurement of and LN edge as total thickness. The observed increase in layer thickness was caused by the reactivity of Li within the intermetallic phase, which reacted with N_2 in addition to the vapor deposited Li. Overall, a homogeneously distributed LN and LZLN layer on Li_{rp} metal foil was deposited by thermal evaporation and/or gas treatment. The corresponding layer thicknesses and consistency of the layers were determined by means of cryogenic cross-sections and the EDX analysis revealed the presence of the LiZn and LN layer.

Time-of-flight secondary-ion mass spectrometry (ToF-SIMS) depth profiling was employed to further investigate and confirm the composition of the single LN and dual LZLN layer and to assess the transition of interfaces. Fig. 3 shows the ToF-SIMS sputter depth profiles and the corresponding 3D reconstructions of the Li_{LN} or Li_{LZLN}.

On the surface of the Li_{LN} (Fig. 3a) a Li_4N^+ fragment (I, red) was detected, assigned to the deposited LN layer. As sputtering continued, the Li_4N^+ intensity decreased while the Si^- intensity increased (II, green). The Si^- fragment indicated that the top surface of Li_{rp} was reached and derived from the siliconized Mylar foil, used as release liner during roll-pressing of the Li metal foil. A decrease in the Si^- intensity was accompanied by an increase in the Ar_3^+ intensity (II, black). The Ar_3^+ fragment was interpreted as an indicator of Li metal foil due to the integration of Ar^+ ions into the Li metal surface during sputtering. The described assignment of the Si^- and Ar_3^+ fragments was also reported by Mense *et al.* in a previous study regarding ToF-SIMS sputter depth profiling of Li metal electrodes.[45] Fig. 3b illustrates the depth profile of Li_{LZLN}. First, the Li_4N^+ fragment (I, red) was detected on the outer surface and implied the presence of the LN layer. A higher sputter ion dose was required to sputter through the LZLN layer and indicated a thicker LN layer for the dual layer compared to the single layer. The thicker LN layer was also observed in the cross-section images of Li_{LZLN} as compared to Li_{LN} (LN layer: Fig. 2f, LZLN layer: Fig. 2i). The LN layer was followed by an underlying layer represented by a $LiZn^+$ fragment (II, yellow, Fig. 3b) with an unexpectedly low intensity, but co-located with a more intense Li_x^+ fragment ($x = 7-9$, II, blue, Fig. 3b).[45] The $LiZn^+$ and Li_x^+ fragments measured below were associated to the LiZn intermetallic phase as described by Mense *et al.*[45] The observed low intensities for the $LiZn^+$ fragment in the intermetallic phase are likely attributed to matrix-effects during the SIMS ionization process. Since Li has a lower electronegativity compared to Zn it may get preferentially ionized in the collision process resulting in the observed behavior.[45] Below the described dual layer consisting of a LN and LiZn layer, the Si^- intensity maximum (III, green, Fig. 3b) with subsequent increase of the Ar_3^+ intensity (III, black, Fig. 3b) indicated the Li_{rp} metal surface. 3D reconstruction of the depth profiles from Li_{LN} and Li_{LZLN} were generated (Fig. 3c and d) and the individual spatial distributions of selected secondary ions are displayed in Fig. S4.† The homogeneous distribution of the LN layer on the outer surface and the thicker LN layer on top of the LiZn intermetallic layer were visualized for both Li_{LN} and Li_{LZLN} in 3D reconstruction (Fig. 3c and d). Underneath the LN layer, detected by the Li_4N^+ signal (red), the Li bulk (Ar_3^+ signal, grey, Fig. 3c) or the intermetallic phase ($LiZn^+$ and Li_x^+ signal, blue, Fig. 3d) is illustrated. Consequently, the individual components of the LN and LZLN layer were confirmed using ToF-SIMS analysis. The sputter ion dose spectra offered a detailed analysis of the single components and the impact of the roll-pressing method, while the 3D reconstructions provided a clear overview of the main fragments (Li_4N^+, LiZn, Li_x^+, Ar_3^+).

Raman spectroscopy was further employed to verify the formation of the LN layer *via* gas phase reaction, since the EDX and ToF-SIMS analysis solely verified the components of the individual compounds (Zn and Li for LiZn; N for LN). Fig. S6† shows the Raman spectra of the LN layer on Li_{rp}, Li_3N powder and Li_{rp} as reference samples. The signal at 1845 cm^{-1} was assigned to the C–C-triple bond of a carbide species, which was formed as a decomposition product of Li_2CO_3 from laser irradiation during the measurement and was also observed in the Li_{rp} reference spectra (Fig. S5a and c†).[51] Due to the fact that the LN layer on Li_{rp} is relatively thin (100 nm), the underlying native layer was reduced by the laser beam and Li_2C_2 was detected. A characteristic band at 515 cm^{-1}, 575 cm^{-1} and 610 cm^{-1} and a broad band from 930 cm^{-1} to 1375 cm^{-1} was observed for the

 This journal is © The Royal Society of Chemistry 2025

Open Access Article. Published on 14 januar 2025. Downloaded on 28.8.2025 23:04:52.
This article is licensed under a Creative Commons Attribution 3.0 Unported Licence.

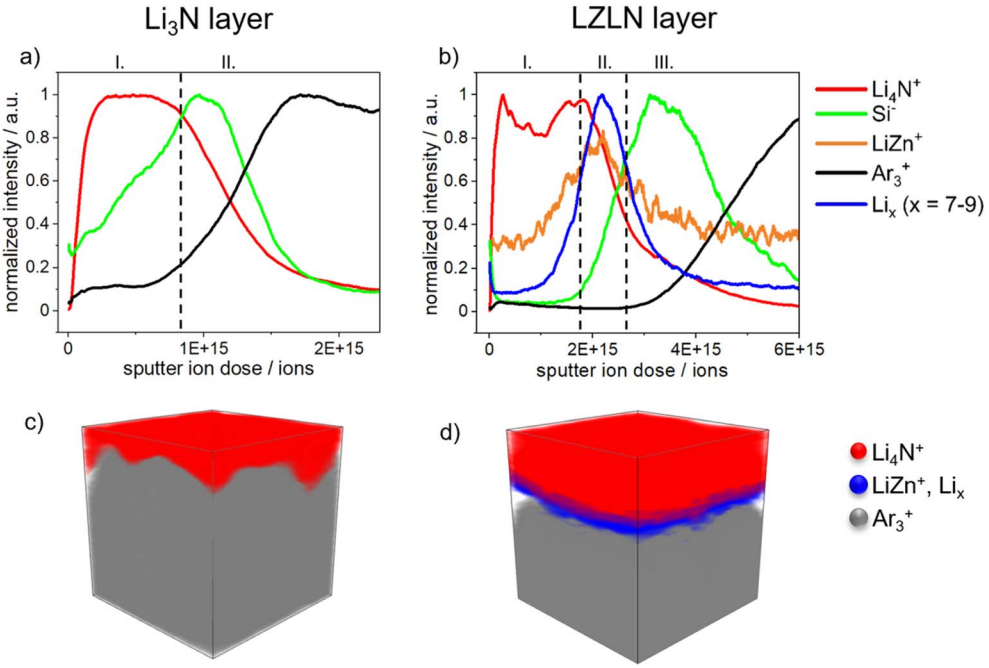

Fig. 3 Normalized ToF-SIMS depth profiles reveal the surface composition of (a) Li_{LN} and (b) Li_{LZLN}. 3D reconstruction of the sputtered area (100 × 100 μm^2) corresponding to the depth profiles show the composition of (c) Li_{LN} and (d) Li_{LZLN} with selected secondary ions marked in red: Li_4N^+, blue: $LiZn^+$ and Li_x^+ (x = 7–9) and grey: Ar_3^+.

LN layer on Li_{rp} (Fig. S5a†). The characteristic and broad band was assigned to the Li_3N species, because both signals were detected in the Li_3N powder reference spectra (Fig. S5b†). In summary, the analysis of the LN layer on Li_{rp} by Raman spectroscopy supported the conclusion that Li_3N was formed as a top layer through comparison with Li_3N powder and Li_{rp} as a reference material.

The LN and LZLN protective layers were electrochemically analyzed in a symmetric cell setup with $Li_{LN}||Li_{LN}$ (red) and $Li_{LZLN}||Li_{LZLN}$ (blue) electrode configurations and compared to $Li_{rp}||Li_{rp}$ (grey) as a reference. The beneficial influence of the LN and LZLN layer was observed in the long-term cycling experiment at different current densities (Fig. 4a and b). Notably, the cycling stability was increased with both LN and LZLN layer compared to bare Li_{rp} before reaching the cut-off voltage, due to an enhanced protection of the Li bulk and an improved homogeneity during Li electrodeposition/-dissolution. This trend was observed for low, moderate and high current densities (Fig. 4a for 0.5 mA cm^{-2}, Fig. 4b for 1.0 mA cm^{-2}, Fig. S6† for 2.0 mA cm^{-2}). At moderate current density of 1.0 mA cm^{-2}, an 80% increase in cycle number before reaching the cut-off voltage was reached for symmetric cells built with Li_{LZLN} compared to Li_{rp} (from Table S1:† Li_{rp}: 200 cycles, Li_{LZLN}: 360 cycles), compared to a 42% increase at higher current densities of 2.0 mA cm^{-2} (Fig. S6 and Table S1†). The Li_{LN} electrodes showed an improved cycling stability compared to Li_{rp}, but a reduced cycling stability compared to the Li_{LZLN} electrodes for the three investigated current densities (Fig. 4a, b, S6 and Table S1†). Fig. 4c–e emphasizes the electrodeposition/-dissolution behavior of symmetric cells with $Li_{rp}||Li_{rp}$, $Li_{LN}||Li_{LN}$ and $Li_{LZLN}||Li_{LZLN}$ at different cycling stages with a fixed current density of 1.0 mA cm^{-2}. The voltage profile of $Li_{rp}||Li_{rp}$ is magnified in Fig. 4c and shows a small peak at the beginning of the first half cycle and a larger one at the end. The first peak was associated to the nucleation of Li ions onto HSAL at the Li surface.[10] Since a large volume of HSAL accumulated after 75 cycles at the Li electrode surface, the energy barrier for nucleation was low (Fig. S7†). Once the initial kinetic barrier for Li ion deposition on existing HSAL was overcome (first peak), there was a continuous deposition of Li ions onto the surface, leading to a decrease in overvoltage (area between the first and second peak). The second peak demonstrated a higher energy barrier for electrodissolution, as Li ions need to dissolve from the Li bulk and diffuse through a porous layer consisting of mossy HSAL and a dead Li layer.[10,52,53] After advanced electrodeposition/-dissolution, the second peak becomes more dominant and the overvoltage for the $Li_{rp}||Li_{rp}$ cell continued to increase until the cut-off voltage was reached after 200 cycles. $Li_{LN}||Li_{LN}$ and $Li_{LZLN}||Li_{LZLN}$ showed a similar voltage profile for the initial charge/discharge cycling phase compared to $Li_{rp}||Li_{rp}$. With increasing cycle number, the voltage profile turned into an arc profile followed by a plateau for each half cycle (Fig. 4c–e). The arcing behavior reflects the state of facilitated Li ion deposition, resulting from a reduced kinetic barrier due to an enhanced Li ion diffusion through the protective layer or the Li ion deposition on HSAL. The plateau profile characterizes a facilitated growth of HSAL at the negative electrode and dissolution from HSAL/pits from the positive electrode. This voltage profile was stable for an extended cycling period, while an overall increase in overvoltage was observed.[10,52] The increase

Open Access Article. Published on 14 januar 2025. Downloaded on 28.8.2025 23:04:52.
This article is licensed under a Creative Commons Attribution 3.0 Unported Licence.

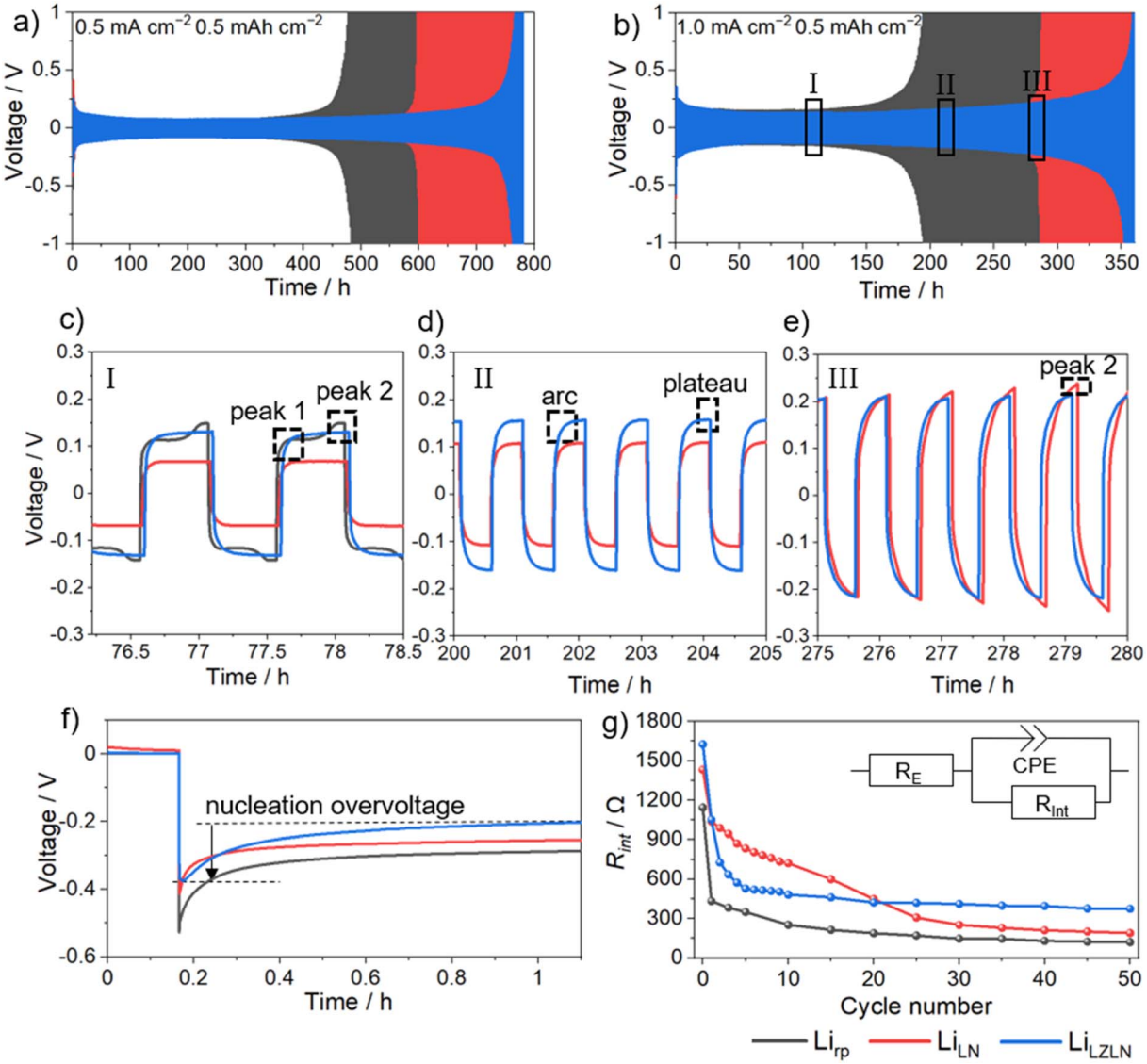

Fig. 4 Galvanostatic cycling of symmetric $Li_{rp}||Li_{rp}$ (grey), $Li_{LN}||Li_{LN}$ (red) and $Li_{LZLN}||Li_{LZLN}$ (blue) cells at a fixed current density of (a) 0.5 mA cm^{-2} and (b) 1.0 mA cm^{-2} with a capacity of 0.5 mA h cm^{-2}. (c)–(e) Emphasizes the electrodeposition/-dissolution behavior from (b) of $Li_{rp}||Li_{rp}$, $Li_{LN}||Li_{LN}$ and $Li_{LZLN}||Li_{LZLN}$ after (c) 75, (d) 200 and (e) 275 cycles at a current density of 1.0 mA cm^{-2}. (f) Nucleation overvoltage profiles from the first electrodeposition at 0.5 mA cm^{-2}. (g) R_{int} evolution determined by EIS within the first 50 cycles at 0.5 mA cm^{-2}.

in overvoltage for the arc and following plateau profile with advanced electrodeposition/-dissolution was associated to limited Li ion diffusion processes through the protective layer or HSAL/dead Li accumulation at the surface, as the diffusion pathway through the HSAL/dead Li layer was growing. The observed arc and plateau profile for $Li_{LN}||Li_{LN}$ and $Li_{LZLN}||Li_{LZLN}$ was associated to the Li ion diffusion through the single or dual protective layer (Fig. 4c and d). Fig. 4e displays a less dominant plateau and an increase in the second peak overvoltage at higher cycle numbers, which indicated that Li ions need to overcome a larger volume of HSAL and more energy is required for Li ion dissolution from Li bulk at the positive electrode. Overall, the long-term cycling experiment revealed an extended cycle life for symmetric cells with dual layer protected Li_{rp} electrodes compared to Li_{rp} or single layer protection. A detailed analysis of the overvoltage profiles showed a facilitated and more homogeneous Li electrodeposition/-dissolution behavior with single and dual layer protected Li_{rp}, which was accompanied with a decelerated consumption of the Li bulk.

In order to gain further insight into the Li ion diffusion through the Li_3N and LZLN dual layer on Li_{rp}, the nucleation overvoltage of the initial Li electrodeposition and interphase resistance R_{int} within the first 50 cycles was investigated (Fig. 4f and e). The observed nucleation overvoltage provided information about the kinetic hindrance for Li ions to diffuse through either a protective layer or the SEI layer on Li_{rp}. The nucleation overvoltage is defined as the difference between the sharp voltage tip and the flat voltage plateau, as shown in Fig. 4f for a $Li_{LZLN}||Li_{LZLN}$ symmetric cell.[54] $Li_{rp}||Li_{rp}$ has the highest nucleation overvoltage with 0.26 V compared to LN and LZLN

 This journal is © The Royal Society of Chemistry 2025

Open Access Article. Published on 14 januar 2025. Downloaded on 28.8.2025 23:04:52.
This article is licensed under a Creative Commons Attribution 3.0 Unported Licence.

protected Li_{rp} electrodes. This trend was observed due to the formation of a SEI which creates an additional barrier for Li ion electrodeposition. For the protected Li_{rp} electrode, a substantial reduction in nucleation overvoltage was observed. Thus, the nucleation overvoltage dropped to 0.20 V for $Li_{LZLN}||Li_{LZLN}$ and to 0.19 V for $Li_{LN}||Li_{LN}$. The observed nucleation overvoltage decrease was interpreted as either a lowering of the kinetical hindrance for Li ions to diffuse through the protective layer or a deposition of Li ions on top of the protective layer. In order to elucidate the deposition behavior of Li ions by electrochemical analysis, EIS measurements were conducted and analyzed the R_{int} of symmetric cells before and after electrodeposition/-dissolution (Fig. 4g). The R_{int} depends on the Li ion and electron conductivity between the interface and electrolyte and allows an assessment of the protective property and the Li electrodeposition/-dissolution behavior. $Li_{rp}||Li_{rp}$ showed a high R_{int} prior to electrodeposition/-dissolution, due to SEI formation between Li and the electrolyte, followed by a rapid reduction in R_{int} owing to an increased surface area caused by pit formation and HSAL growth.[29,53] R_{int} of $Li_{LN}||Li_{LN}$ and $Li_{LZLN}||Li_{LZLN}$ showed overall a higher value before and during electrodeposition/-dissolution compared to bare Li_{rp}. The increased R_{int} value at 0 cycles for Li_{LN} and Li_{LZLN} was interpreted as a successful protection of Li surface against degradation processes with the electrolyte. However, after repeated charge/discharge cycles, cracking of the LN layer was observed, leading to reduced kinetic hindrance for Li ion deposition, which was observable in the decrease of R_{int} for $Li_{LN}||Li_{LN}$ to a similar R_{int} as for $Li_{rp}||Li_{rp}$. Further cracks in the LN layer, induced by volume changes, lead to accelerated pit formation and HSAL growth in areas of Li electrodeposition/-dissolution. This was indicated by a continuous decrease of R_{int} for $Li_{LN}||Li_{LN}$ from cycle 30 to 50. The $Li_{LZLN}||Li_{LZLN}$ cells showed a R_{int} drop within the first 10 cycles, followed by a virtually constant R_{int} up to 50 cycles. The initial R_{int} drop implied that the LZLN layer was suffering from coating cracks similarly to the LN layer. Yet, during the subsequent cycling period (cycles 10 to 50), the LZLN layer was found to improve the overall stability of both layers. Therefore, it was concluded that the benefits of the dual layer combination are an electronically insulating top layer, more homogeneously distributed nucleation sites due to the LiZn layer, and an overall higher stability towards volume changes (if LN layer cracks, LiZn layer remains protective character). This improvement resulted in a superior protection of the subjacent Li surface from electrolyte decomposition and an improved behavior during Li electrodeposition and dissolution.

The higher stability and improved protection of Li_{LZLN} was verified by SEM top-view and cross-sections with corresponding EDX images after 25 and 50 cycles and compared to bare Li_{rp} and Li_{LN} (Fig. 5).

Fig. 5a–c shows aged Li_{rp}, Li_{LN} and Li_{LZLN} electrode as top-view images after 25 cycles and the area of the cross-section is marked with a red bar. Cross-sections were performed in regions at boundaries between HSAL growth and intact surface to analyze the cracking mechanism of the protective layer on the Li_{rp} surface upon continuous electrodeposition/-dissolution. With repeated electrodeposition/-dissolution, pits are formed and HSAL is deposited on the surface and in the pits. The pits grow deeper with increasing cycle number and were refilled with growing HSAL. The surface analysis of Li_{rp} after 25 cycles proofed the degradation behavior by showing HSAL growth at the surface (Fig. 5a). Cross-section analysis, supported by corresponding EDX images, further demonstrated HSAL penetration in deeper regions (Fig. 5d and g: HSAL in green). HSAL was represented by a mossy/chunk-like morphology and an oxygen signal (green), since Li reacted with the carbonate-based electrolyte to form oxygen-containing species. The LN layer is represented by the associated nitrogen signal (purple) and the intermetallic LiZn layer by the zinc signal (yellow). The top-view image of the Li_{LN} electrode after 25 cycles exhibited HSAL structures on the surface, that cracked the LN layer and penetrated into the Li bulk (Fig. 5b). Cross-section images and corresponding EDX analysis showed pit formation in regions of HSAL growth, while the adjacent LN layer remained intact. The LN layer underneath the HSAL showed a weaker nitrogen signal, indicating the rupture of the rigid layer (Fig. 5h: HSAL in green, Li_3N in purple). The HSAL growth was also observed on the surface of the LZLN layer (Fig. 5b). However, in the top-view image, the LZLN layer appeared undamaged in regions of HSAL growth and an undamaged dual layer was also confirmed by the cross-section image and EDX analysis (Fig. 5f and i). HSAL growth (Fig. 5i, green) was observed on top of the LZLN layer (Fig. 5i, Li_3N: purple, LiZn: yellow), with an intact LZLN layer and no visible cracks in the region of HSAL growth.

After 50 cycles, deeper pit formation and a higher amount of HSAL on top of the Li_{rp} or protected Li_{rp} electrode surface was observed in both SEM and optical images (Fig. 5j–o and S7†). Cross-section images with corresponding EDX analysis of Li_{rp} showed a distinctive HSAL layer with mossy structure (Li_{rp}: Fig. 5j and m). The HSAL layer of the Li_{rp} electrodes was overall less dense and consisted of a thicker layer compared to the protected Li_{rp} electrodes (Li_{rp}: Fig. 5j, Li_{LN}: Fig. 5k, Li_{LZLN}: Fig. 5l). The Li_{LN} electrode showed a cracked LN layer in areas with advanced HSAL growth as a continuous nitrogen signal was absent (Fig. 5k and n). HSAL was found in a higher depth of penetration into the Li bulk with a dominant mossy structure and a few denser Li deposits in predominantly deeper regions (Fig. 5k, denser HSAL deposits framed red). Denser Li deposits are resulting from a better contact of Li ions with the Li bulk during electrodeposition, while they are effectively protected against electrolyte decomposition and SEI formation during the deposition process. Therefore, the cross-section image derived that the LN layer was first intact, causing thicker Li deposits, and with continued cycling, mossy and less dense HSAL was growing due to a ruptured LN layer with less protective properties (Fig. 5k). Cross-section images and EDX analysis of Li_{LZLN} electrodes showed HSAL growth (green) with a mossy structure on top of the protective layer and a higher amount of denser Li deposits below the protective layer compared to Li_{LN} and Li_{rp} electrodes (Fig. 5l and o, denser HSAL deposits framed red). Presumably, the higher amount of denser Li deposits was found, because the LZLN layer featured a higher degree of intact protective properties shielding the Li deposits from electrolyte

Open Access Article. Published on 14 januar 2025. Downloaded on 28.8.2025 23:04:52.
This article is licensed under a Creative Commons Attribution 3.0 Unported Licence.

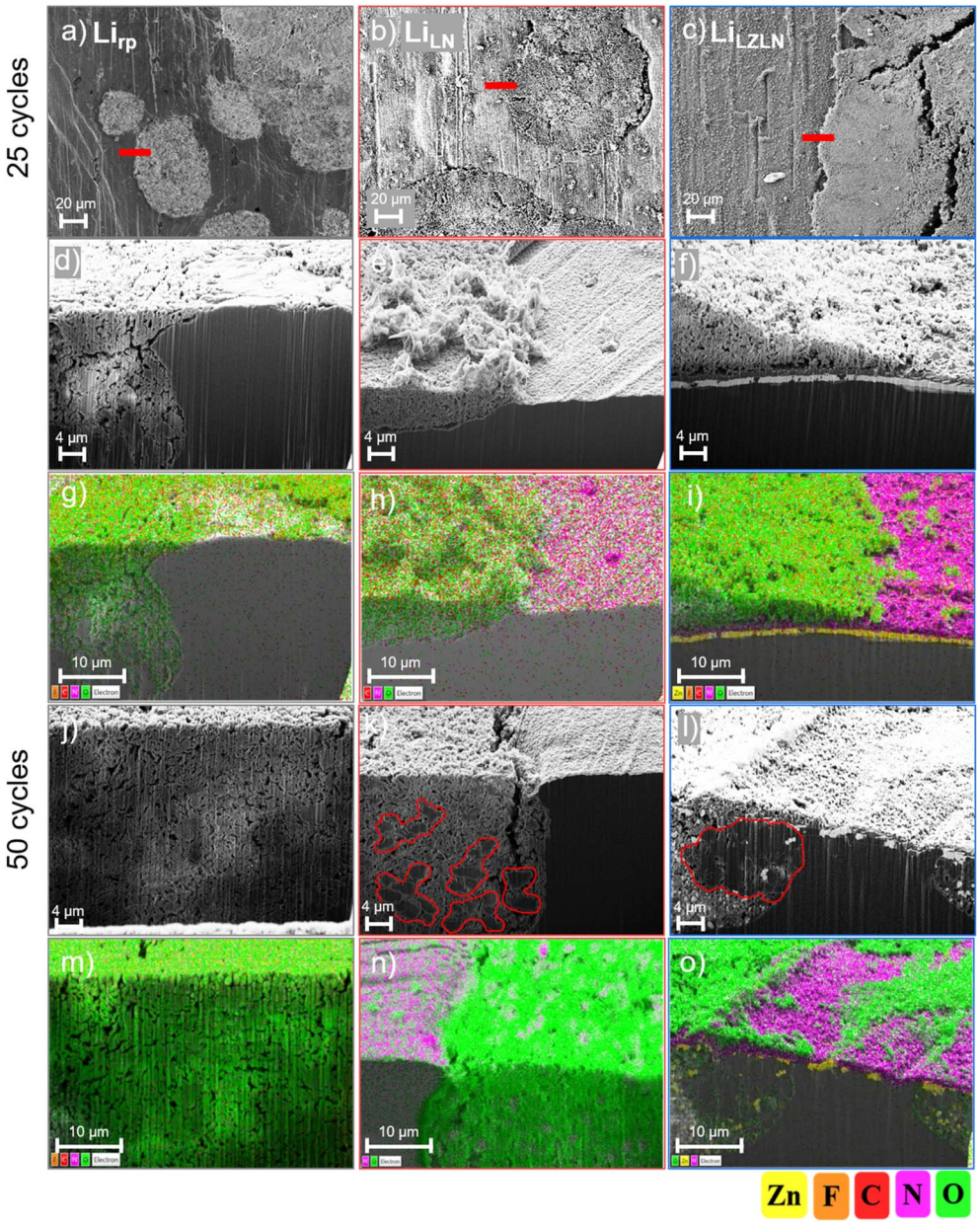

Fig. 5 Top-view SEM images of (a) Li_{rp}, (b) Li_{LN} and (c) Li_{LZLN} electrodes after 25 cycles at 0.5 mA cm^{-2} with red bars that are indicating the cross-section area. The left column belongs to Li_{rp} electrode, the middle column to the Li_{LN} electrode and the right column to the Li_{LZLN} electrode. (d)–(f) Shows the cross-sectional SEM images after 25 cycles and (g)–(i) the corresponding EDX mapping images. (j) and (l) Displays the cross-sectional SEM images after 50 cycles and (m)–(o) the corresponding EDX mapping images. (k) and (l) Display red framed areas that are marking thicker Li deposits.

decomposition. The LiZn layer (Fig. 5o, yellow) was found after 50 cycles with severe cracks and advanced dissolution into HSAL and the Li bulk. However, the LN layer (purple) on top was found as intact layer in regions of HSAL growth above and below the LZLN layer. Consequently, the improved cycling stability of the Li_{LZLN} electrodes during electrodeposition/-dissolution was explained by the morphological analysis. A single intermetallic LiZn layer dilutes into the HSAL and Li bulk during the cycling process and a rigid, single LN layer cracks in certain areas where HSAL growth and pit formation are subsequently facilitated. The described process occurred delayed with the LZLN layer, since the LN layer protects the LiZn layer from early dissolution into HSAL and the LiZn layer homogenizes the Li ion flux during electrodeposition/-dissolution. Based on the results of the cross-section images and the electrochemical analysis, a combination of protective layers with different properties is proposed. This approach aims to reduce the overall thickness of the protective layer while increasing its effectiveness. Thus, the delayed initiation of coating cracks, higher homogeneity of Li ion electrodeposition/-dissolution and a subsequently delayed exposure of the reactive Li bulk resulted in an enhanced cycle life.

 This journal is © The Royal Society of Chemistry 2025

Open Access Article. Published on 14 januar 2025. Downloaded on 28.8.2025 23:04:52.
This article is licensed under a Creative Commons Attribution 3.0 Unported Licence.

After studying the protective layer on Li_{rp} electrodes in symmetric cells and analyzing their morphology before and after cycling through cryogenic cross sections, the next step was to investigate its practical application in NMC622||Li cells. Therefore, NMC622||Li cells with Li_{rp}, Li_{LN} and Li_{LZLN} electrodes were assembled and their practical application in LMBs was investigated. Fig. 6a shows the progression of the specific discharge capacity and coulombic efficiency of the NMC622||Li cells.

The initial capacity of NMC622||Li cells with Li_{rp}, Li_{LN} or Li_{LZLN} as negative electrode was ≈160 mA h g^{-1}, based on the discharge capacity of the positive electrode. Fig. 6a shows a rapid capacity decay of NMC622||Li_{rp} followed by NMC622||Li_{LN} and an enhanced capacity retention with NMC622||Li_{LZLN}. The state of health (SOH) values of 80% are visualized in Fig. 6a. For cells with Li_{rp} as negative electrode the SOH (80%) was reached after 70 cycles, for the ones with Li_{LN} after 71 cycles and for the ones with Li_{LZLN} after 105 cycles. This represented a 50% improvement in SOH (80%) for cells with Li_{LZLN} as a negative electrode compared to the ones with Li_{rp}. The comparatively poor cycle life and accelerated capacity fade of NMC622||Li cells in comparison to Li||Li cells was attributed to the 4–5 times higher areal capacity of the NMC622||Li cells associated with a correspondingly enhanced amount of shuttled lithium.

Post mortem analysis of cycled Li electrodes showed that Li_{rp} has already after 25 cycles a higher HSAL growth and pit formation compared to the coated Li electrodes (Fig. 5d–i). It is therefore reasonable to observe a premature capacity fading for Li_{rp} negative electrodes. However, the discharge capacity of NMC622||Li_{LN} cells showed a similar capacity decay as with Li_{rp} electrodes, emphasizing that a single LN layer with 100 nm layer thickness lacks in a comprehensive Li surface protection in combination with NMC622.

A lower surface protection with was visible in the cross-section images of aged Li_{LN} with a cracked LN layer in regions of HSAL growth after 25 cycles (Fig. 5h). These regions accelerate a rollover failure with continues charge/discharge cycles.[55] The undamaged LZLN layer after 25 cycles and the intact Li_3N layer of the dual layer after 50 cycles (Fig. 5i and o) emphasized the elevated surface protection that was observed in Fig. 6a for NMC622||Li_{LZLN}. The corresponding charge/discharge voltage profile (Fig. 6b) of the initial cycle revealed a similar voltage polarization for Li_{LN} and Li_{LZLN} and a higher polarization for Li_{rp} as negative electrode. The higher polarization of NMC622||Li_{rp} compared to cells with Li_{LN} and Li_{LZLN} electrodes indicated a higher internal resistance and kinetical hindrance for Li ion deposition during charge and for Li ion dissolution during discharge. After 100 cycles, the charge/discharge voltage polarization sharply increased for Li_{rp} and Li_{LN} until reaching 4.2 V, followed by a kink and slower voltage rise. The discharge profile displayed a rapid voltage decline, suggesting low capacity for NMC622 cells equipped with both Li_{rp} and Li_{LN} negative electrodes. In contrast, NMC622||Li_{LZLN} cells retained a classic voltage polarization profile with a lower capacity loss. Overall, the analysis of NMC622||Li cells proved an improved performance of Li_{rp} electrodes with a dual protective LZLN layer compared to single protective LN layer or bare Li_{rp} electrodes.

Conclusion

In this study, a dual protective layer consisting of an intermetallic LiZn bottom layer and an inorganic Li_3N (LN) top layer was fabricated *via* thermal evaporation. The PVD technique offered the possibility of thickness control and high purity of both

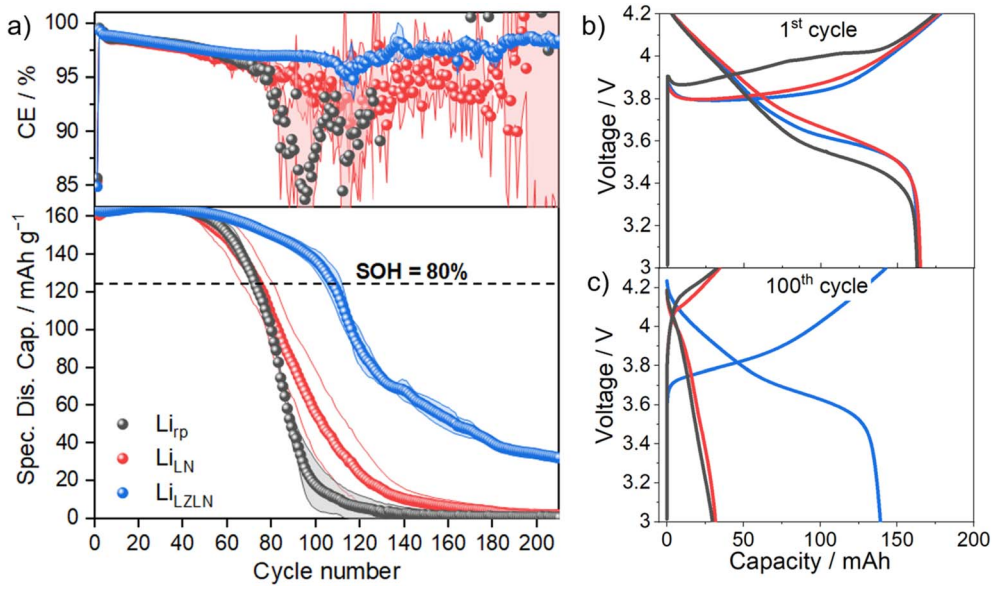

Fig. 6 (a) Electrochemical performance of NMC622||Li cells with Li_{rp} (grey), Li_{LN} (red) or Li_{LZLN} (blue) electrodes as negative electrode. (a) Capacity retention and the coulombic efficiency in a long-term cycling experiment at 0.2C. (b) The corresponding charge/discharge voltage profiles after initial cycle and (c) after 100 cycles.

Open Access Article. Published on 14 januar 2025. Downloaded on 28.8.2025 23:04:52.
This article is licensed under a Creative Commons Attribution 3.0 Unported Licence.

deposited layers. The selection of the LiZn layer was based on its high Li ion diffusion coefficient, which reduces nucleation overvoltage and promotes a uniformly distributed electrodeposition of Li ions. The Li_3N layer was chosen as the top layer for its high Li ion and low electronic conductivity, encouraging Li ions to deposit under the protective layer. SEM, EDX and ToF-SIMS analysis revealed a homogeneously distributed and a well-defined LiZn and LN layer. Intensive analysis of the protected surface before and after cycling by SEM, in particular cross-sections under cryogenic conditions, revealed the reason for the increased protection of the Li metal surface provided by the LZLN layer. Compared to the Li_{rp} surface or LN layer, which showed a cracked surface, pit formation and HSAL growth, the LZLN dual layer presented an intact coating with absence of cracks in areas of HSAL growth. In fact, even after 50 cycles, the LZLN layer was still intact, with the intermetallic layer starting to dissolve into HSAL and Li bulk. Electrochemical analysis revealed an 80% increase in cycle life for symmetric cells and a 50% increase in SOH (80%) for NMC622||Li cells with Li_{LZLN} as negative electrode compared to the ones with Li_{rp}. Overall, an enhanced cycling performance for both symmetric Li||Li cells and NMC622||Li cells was demonstrated with the LZLN protected Li_{rp} electrodes. The performance increase resulted from a mitigation of premature cracking of the brittle Li_3N layer due to a more homogeneously distributed Li ion electrodeposition/dissolution attributed the LiZn layer. Additionally, the Li_3N layer inhibited an accelerated dissolution of the LiZn layer into HSAL and Li bulk during cycling. In combination, the LZLN layer produced a superior protection of the Li surface and an improved Li electrodeposition/-dissolution behavior.

In conclusion, this study highlights the synergistic effects achieved by combining protective layers with diverse properties, leading to a noteworthy improvement in the cycle lifetime of Li||Li and NMC622||Li cells. The study of aged coated/uncoated Li electrodes exhibited the importance in understanding how coating degradation leads to a subsequent capacity loss. Especially the *post mortem* morphology-preserving analyses of protective layers demonstrated that the failure analysis is essential for a continuous improvement regarding coating development on Li electrodes for symmetric cells, full cells, but also for future investigations involving solid-state batteries. For further thickness optimization of dual protective layers, combined simulation calculations and insights into performance behavior of protective layers from experimental data could be used for predicting the optimal design of next-generation lithium metal anodes.

Data availability

The data supporting this article have been included as part of the ESI.†

Author contributions

A. Bar for creating the graphical illustration. S. Greiwe co-developed the Li_3N layer as a part of a master thesis and performed Raman spectroscopy for characterization; M. Mense: performed ToF-SIMS measurements, analyzed and discussed the results with M. M. Bela; M. C. Stan: discussion and supervision; M. Börner, M. Winter: discussion, supervision, proofreading, contribution to the final draft, and acquisition of funding. All authors were involved in the discussion of the results and approval of the final manuscript.

Conflicts of interest

The authors declare no conflicts of interest.

Acknowledgements

Financial support provided by the EU Horizon Europe – research and innovation action within the research project "PSIONIC" (101069703) and the German Federal Ministry of Education and Research (BMBF) within the research project "ProLiFest" (03XP0253A) is gratefully acknowledged.

References

1 R. Schmuch, R. Wagner, G. Hörpel, T. Placke and M. Winter, *Nat. Energy*, 2018, **3**(4), 267.
2 M. S. Whittingham, *Chem. Rev.*, 2014, **114**(23), 11414.
3 J. B. Goodenough and K.-S. Park, *J. Am. Chem. Soc.*, 2013, **135**(4), 1167.
4 T. Placke, R. Kloepsch, S. Dühnen and M. Winter, *J. Solid State Electrochem.*, 2017, **21**(7), 1939.
5 J. Liu, Z. Bao, Y. Cui, E. J. Dufek, J. B. Goodenough, P. Khalifah, Q. Li, B. Y. Liaw, P. Liu, A. Manthiram, Y. S. Meng, V. R. Subramanian, M. F. Toney, V. V. Viswanathan, M. S. Whittingham, J. Xiao, W. Xu, J. Yang, X.-Q. Yang and J.-G. Zhang, *Nat. Energy*, 2019, **4**(3), 180.
6 E. Peled, *J. Electrochem. Soc.*, 1979, **126**, 2047.
7 M. Winter, *Zeitschrift für Physikalische Chemie*, 2009, **223**, 1395.
8 E. Peled and S. Menkin, *J. Electrochem. Soc.*, 2017, **164**(7), A1703.
9 D. Aurbach, *J. Power Sources*, 2000, **89**(2), 206.
10 K. N. Wood, E. Kazyak, A. F. Chadwick, K.-H. Chen, J.-G. Zhang, K. Thornton and N. P. Dasgupta, *ACS Cent. Sci.*, 2016, **2**(11), 790.
11 D. Lin, Y. Liu and Y. Cui, *Nat. Nanotechnol.*, 2017, **12**, 194.
12 L. Hellweg, T. Beuse, M. Winter and M. Börner, *J. Electrochem. Soc.*, 2023, **170**(4), 040530.
13 J. Heine, P. Hilbig, X. Qi, P. Niehoff, M. Winter and P. Bieker, *J. Electrochem. Soc.*, 2015, **162**(6), A1094.
14 H. Zhang, G. Gebresilassie Eshetu, X. Judez, C. Li, L. M. Rodriguez-Martínez and M. Armand, *Angew. Chem., Int. Ed.*, 2018, **57**, 5002.
15 Y.-G. Lee, S. Fujiki, C. Jung, N. Suzuki, N. Yashiro, R. Omoda, D.-S. Ko, T. Shiratsuchi, T. Sugimoto, S. Ryu, J. H. Ku, T. Watanabe, Y. Park, Y. Aihara, D. Im and I. T. Han, *Nat. Energy*, 2020, **5**(4), 299.
16 M.-H. Ryou, Y. M. Lee, Y. Lee, M. Winter and P. Bieker, *Adv. Funct. Mater.*, 2015, **25**(6), 834.

 This journal is © The Royal Society of Chemistry 2025

Open Access Article. Published on 14 januar 2025. Downloaded on 28.8.2025 23:04:52.
This article is licensed under a Creative Commons Attribution 3.0 Unported Licence.

17 H. Wang, Y. Liu, Y. Li and Y. Cui, *Electrochem. Energy Rev.*, 2019, **2**(4), 509.
18 N. Delaporte, Y. Wang and K. Zaghib, *Front. Mater.*, 2019, **6**, 267.
19 D. Kang, M. Xiao and J. P. Lemmon, *Batteries Supercaps*, 2020, **4**(3), 445.
20 J. Wellmann, J.-P. Brinkmann, B. Wankmiller, K. Neuhaus, U. Rodehorst, M. R. Hansen, M. Winter and E. Paillard, *ACS Appl. Mater. Interfaces*, 2021, **13**(29), 34227.
21 D. G. Belov, O. V. Yarmolenko, A. Peng and O. N. Efimov, *Synth. Met.*, 2006, **156**(9–10), 745.
22 M. Wu, Z. Wen, Y. Liu, X. Wang and L. Huang, *J. Power Sources*, 2011, **196**(19), 8091.
23 Y. J. Zhang, W. Wang, H. Tang, W. Q. Bai, X. Ge, X. L. Wang, C. D. Gu and J. P. Tu, *J. Power Sources*, 2015, **277**, 304.
24 Z. Li, S. Santhanagopalan and A. Zakutayev, *MRS Commun.*, 2022, **12**(3), 352.
25 S. Stuckenberg, M. M. Bela, C. T. Lechtenfeld, M. Mense, V. Küpers, T. T. K. Ingber, M. Winter and M. C. Stan, *Small*, 2023, **2305203**, 1.
26 Y. Li, Y. Sun, A. Pei, K. Chen, A. Vailionis, Y. Li, G. Zheng, J. Sun and Y. Cui, *ACS Cent. Sci.*, 2017, **4**(1), 97.
27 M. C. Stan, J. Becking, A. Kolesnikov, B. Wankmiller, J. E. Frerichs, M. R. Hansen, P. Bieker, M. Kolek and M. Winter, *Mater. Today*, 2020, **39**, 137.
28 J. Deng, Y. Wang, S. Qu, Y. Liu, W. Zou, F. Zhou, A. Zhou and J. Li, *Batteries Supercaps*, 2020, **4**(1), 140.
29 M. M. Bela, C. Schmidt, K. Neuhaus, T. Hering, M. C. Stan, M. Winter and M. Börner, *Adv. Mater. Interfaces*, 2024, 2300836.
30 N. Delaporte, A. Perea, S. Collin-Martin, M. Léonard, J. Matton, V. Gariepy, H. Demers, D. Clément, E. Rivard and A. Vijh, *Batteries Supercaps*, 2022, **5**, e202200245.
31 S. Lee, K.-s. Lee, S. Kim, K. Yoon, S. Han, M. H. Lee, Y. Ko, J. H. Noh, W. Kim and K. Kang, *Sci. Adv.*, 2022, **8**(30), 1.
32 Y. Yang, L. Ai, J. He, C. Zhang, D. Chen and L. Shen, *Chem. Commun.*, 2023, **59**, 936–939.
33 S. Wang, J. Chen, H. Lu, Y. Zhang, J. Yang, Y. Nuli and J. Wang, *ACS Appl. Energy Mater.*, 2021, **4**(11), 13132.
34 J. Wang, J. Yang, Q. Xiao, J. Zhang, T. Li, L. Jia, Z. Wang, S. Cheng, L. Li, M. Liu, H. Liu, H. Lin and Y. Zhang, *Adv. Funct. Mater.*, 2020, **31**(7), 2007434.
35 S. Lobe, A. Bauer, S. Uhlenbruck and D. Fattakhova-Rohlfing, *Adv. Sci.*, 2021, **8**(11), 2002044.
36 M. Nicolaus and M. Schäpers, *Modern Surface Technology*, Wiley-VCH Verlag GmbH & Co. KGaA, Weinheim, 2006.
37 D. M. Mattox, *Handbook of Physical Vapor Deposition (PVD) Processing*, Elsevier Science, 2nd edn, 2010.
38 J. Wang, P. King and R. A. Huggins, *Solid State Ionics*, 1985, **20**, 185.
39 A. Anani, S. Crouch-Baker and R. A. Huggins, *Measurement of lithium diffusion in several binary lithium alloys at ambient temperature*, The Electrochemical Society, United States, 1986, http://inis.iaea.org/search/search.aspx?orig_q=RN:18093564.
40 R. A. Huggins, *J. Power Sources*, 1999, **81–82**, 13.
41 S.-K. Otto, T. Fuchs, Y. Moryson, C. Lerch, B. Mogwitz, J. Sann, J. Janek and A. Henss, *ACS Appl. Energy Mater.*, 2021, **4**(11), 12798.
42 C. Zhu, T. Fuchs, S. A. L. Weber, F. H. Richter, G. Glasser, F. Weber, H.-J. Butt, J. Janek and R. Berger, *Nat. Commun.*, 2023, **14**, 1300.
43 J. Becking, A. Gröbmeyer, M. Kolek, U. Rodehorst, S. Schulze, M. Winter, P. Bieker and M. C. Stan, *Adv. Mater. Interfaces*, 2017, **4**(16), 1700166.
44 R. Nölle, K. Beltrop, F. Holtstiege, J. Kasnatscheew, T. Placke and M. Winter, *Mater. Today*, 2020, **32**, 131.
45 M. Mense, M. M. Bela, S. P. Kühn, I. Cekic-Laskovic, M. Börner, S. Wiemers-Meyer, M. Winter and S. Nowak, *Commun. Chem.*, 2025, DOI: 10.1038/s42004-025-01426-0.
46 S.-K. Otto, Y. Moryson, T. Krauskopf, K. Peppler, J. Sann, J. Janek and A. Henss, *Chem. Mater.*, 2021, **33**(3), 859.
47 E. Zintl and G. Brauer, *Zeitschrift für Elektrochemie und angewandte physikalische Chemie*, 1935, **41**(2), 102.
48 A. Rabenau and H. Schulz, *J. Less-Common Met.*, 1976, **50**(1), 155.
49 K. Park and J. B. Goodenough, *Adv. Energy Mater.*, 2017, **7**(19), 1700732.
50 A. D. Pelton, *J. Phase Equilib. Diffus.*, 1991, **12**, 42.
51 R. Schmitz, R. Müller, S. Krüger, R. W. Schmitz, S. Nowak, S. Passerini, M. Winter and C. Schreiner, *J. Power Sources*, 2012, **217**, 98.
52 K.-H. Chen, K. N. Wood, E. Kazyak, W. S. LePage, A. L. Davis, A. J. Sanchez and N. P. Dasgupta, *J. Mater. Chem. A*, 2017, **5**, 11671.
53 G. Bieker, M. Winter and P. Bieker, *Phys. Chem. Chem. Phys.*, 2015, **17**, 8670.
54 R. Zhang, X.-R. Chen, X. Chen, X.-B. Cheng, X.-Q. Zhang, C. Yan and Q. Zhang, *Angew. Chem., Int. Ed.*, 2017, **56**(27), 7764.
55 S. Klein, P. Bärmann, L. Stolz, K. Borzutzki, J.-P. Schmiegel, M. Börner, M. Winter, T. Placke and J. Kasnatscheew, *ACS Appl. Mater. Interfaces*, 2021, **13**(48), 57241.